Title	Beam-based compensation of extracted-beam displacement caused by field ringing of pulsed kicker magnets in the 3 GeV rapid cycling synchrotron of the Japan Proton Accelerator Research Complex
Author(s)	Harada Hiroyuki, Saha P. K., Tamura Fumihiko, Meigo Shinichiro, Hotchi Hideaki, Hayashi Naoki, Kinsho Michikazu, Hasegawa Kazuo
Citation	Progress of Theoretical and Experimental Physics, 2017(9), 093G01 (2017).
Text Version	publisher
URL	https://jopss.jaea.go.jp/search/servlet/search?5060333
DOI	https://doi.org/10.1093/ptep/ptx125
Right	Originally published in Progress of Theoretical and Experimental Physics, 2017, 9, 093G01 © The Author(s) 2017. Published by Oxford University Press on behalf of the Physical Society of Japan. This is an Open Access article distributed under the terms of the Creative Commons Attribution License (http://creativecommons.org/licenses/by/4.0/), which permits unrestricted reuse, distribution, and reproduction in any medium, provided the original work is properly cited.

PTEP

Prog. Theor. Exp. Phys. **2017**, 093G01 (16 pages)
DOI: 10.1093/ptep/ptx125

Beam-based compensation of extracted-beam displacement caused by field ringing of pulsed kicker magnets in the 3 GeV rapid cycling synchrotron of the Japan Proton Accelerator Research Complex

Hiroyuki Harada*, Pranab Kumar Saha, Fumihiko Tamura, Shin-ichiro Meigo, Hideaki Hotchi, Naoki Hayashi, Michikazu Kinsho, and Kazuo Hasegawa

J-PARC Center, Japan Atomic Energy Agency (JAEA), 2-4 Shirakata Shirane, Tokaimura, Nakagun Ibaraki 319-1195 Japan
*E-mail: hharada@post.j-parc.jp

Received June 5, 2017; Revised July 16, 2017; Accepted August 6, 2017; Published September 25, 2017

Commissioned in October 2007, the 3 GeV rapid cycling synchrotron (RCS) of the Japan Proton Accelerator Research Complex was designed for a high-intensity output beam power of 1 MW. The RCS extracts 3 GeV proton beams of two bunches by using eight pulsed kicker magnets and three DC septum magnets with 25 Hz repetition. These beams are delivered to a materials and life science experimental facility (MLF) and a 50 GeV main ring synchrotron (MR). However, the flat-top fields of the kicker magnets experience ringing that displaces the position of the extracted beam. This displacement is a major issue from the viewpoint of target integrity at the MLF and emittance growth at MR injection. To understand the flat-top uniformity of the total field of all the kickers, the uniformity was measured as the displacement of the extracted beams by using a shorter bunched beam and scanning the entire trigger timing of the kickers. The beam displacement of the first bunch exceeded the required range. Therefore, we performed beam-based measurements kicker by kicker to understand each field-ringing effect, and then we understood the characteristics (strength and temporal structure) of each ringing field. We managed to cancel out the ringing by using all the beam-based measurement data and optimizing each trigger timing. As a result, the field-ringing effect of the kickers was successfully compensated by optimizing the trigger timing of each kicker without hardware upgrades or improvements to the kicker system. By developing an automatic monitoring and correction system, we now have a higher stability of extracted beams during routine user operation. In this paper, we report our procedure for ringing compensation and present supporting experimental results.

Subject Index G02, G05, G12

1. Introduction

The Japan Proton Accelerator Research Complex (J-PARC) is a multi-purpose proton accelerator facility [1] comprising three accelerators, namely a 400 MeV H^- linear accelerator (LINAC), a 3 GeV rapid cycling synchrotron (RCS), and a 50 GeV main ring synchrotron (MR), and three experimental facilities, namely a materials and life science experimental facility (MLF), a hadron experimental hall (HD), and a neutrino beam line (NU) for the Tokai to Kamioka Long Baseline Neutrino Oscillation Experiment (T2K). In this chain of accelerators, the RCS accumulates a 400 MeV proton beam through multi-turn injection by exchanging a beam of negative hydrogen ions (H^-) from the LINAC, accelerates the accumulated proton beam to 3 GeV in 20 ms, and simultaneously

delivers 3 GeV proton beams at a high repetition rate of 25 Hz. The RCS acts as both a proton driver to produce pulsed muons and neutrons for the MLF and an injector to the MR, aiming at an output beam power of 1 MW.

The beam commissioning of the J-PARC has proceeded as planned since November 2006, from the LINAC to the downstream facilities. The RCS was commissioned in October 2007 and became available for user operation in December 2008 with an output beam power of 4–20 kW. The output beam power from the RCS in routine user operation has steadily increased following low/high-intensity beam tunings, hardware improvements, and realistic numerical beam simulations [2–4]. Following a series of LINAC injector upgrades in 2013 and 2014, the RCS finally attained all of its design parameters. Thus, in October 2014, beam tuning began on the RCS to achieve the designed 1 MW intensity. In the beam tuning, the RCS has successfully achieved beam acceleration and extraction of 1 MW equivalent intensity, and we achieved an output beam power of 500 kW in routine user operation [5].

In a storage or synchrotron ring that uses fast extraction, pulsed kicker magnets are used to extract the circulating bunched beams. The rise time of the magnetic field should be short enough to complete the generation of the requested magnetic field between the circulating bunches. On the other hand, the flat top of the magnetic field should be long enough to kick all the required bunches and flat enough to keep them on the same extraction orbit.

The RCS extraction system consists of eight pulsed kicker magnets and three direct-current (DC) septum magnets. Unfortunately, ringing in the flat-top fields of the pulsed kicker magnets displaces the extracted beam horizontally. In the design stage of the RCS, the field flatness was required to be within $\pm 1\%$. However, MLF users and MR operators during high-intensity operation required a higher quality for the extracted beams to reduce the risk of target problems and to suppress the associated emittance growth when the beam was injected, respectively. An example of the target problems is that the mercury target vessel may crack or even break when the beam power is ramped up [6]. Although this is mainly a target-construction problem, higher beam quality and stability on the target would reduce the risk. An example of the issues affecting MR injection is that the injection-beam displacement directly increases the emittance of the circulating beam in the MR just where beam loss is most likely, thereby limiting the MR beam power. Therefore, a key issue for operating the RCS at higher intensity is to improve the quality and stability of the extracted beams.

In this paper, we propose a method for evaluating the field ringing and the extracted-beam displacement. We present a way to compensate for kicker ringing, as well as results that show that it leads to a higher-quality extracted beam, together with introduction of the kicker system configuration and field ringing at the RCS. Additionally, we present an online system for monitoring and correcting the kicker timing for a more stable extracted beam and to address a problem due to the output current drift of the kicker.

2. RCS layout and design parameters

Figure 1 shows a schematic view of the RCS, the design parameters of which are listed in Table 1. Details of the distinctive features of the RCS devices are described in Ref. [7]. As shown in Fig. 1, a H^- beam from the LINAC is delivered via the LINAC-to-3 GeV beam transport line (L-3BT) to the RCS injection point, where it is multi-turn charge-exchange injected through hybrid-type boron-mixed carbon stripping foil (called HBC foil [8]) with a thickness of 330 μg/cm^2 over a beam injection period of 0.5 ms. To avoid longitudinal beam loss during beam injection and acceleration, the injected H^- LINAC beam is equipped with a chopped-bunch structure synchronized at the ring

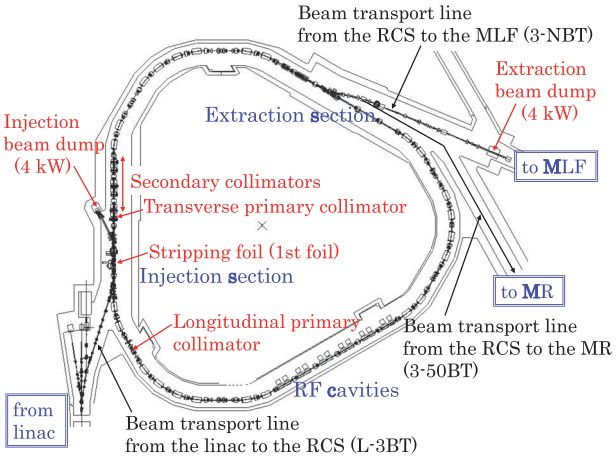

Fig. 1. Schematic view of the RCS.

Table 1. RCS design parameters.

Circumference	348.333 m
Superperiodicity	3
Injected beam:	
particles	H^-
energy	400 MeV
transverse emittance (unnormalized)	4π mm mrad
momentum spread	$\pm 0.1\%$
Injection period	0.5 ms (307 turns)
Extraction energy	3 GeV
Repetition rate	25 Hz
Ramping pattern	Sinusoidal
Harmonic number	2
Number of bunches	2
Number of particles per pulse	8.3×10^{13}
Output beam power	1 MW
Ring collimator capability	4 kW
Betatron horizontal/vertical tune	6.45/6.42
Natural horizontal/vertical chromaticity	$-8.5/-8.8$
Transition energy	9.2 GeV
Transverse acceptance:	
ring aperture	486π mm mrad
collimator aperture (set)	324π mm mrad
Ring momentum acceptance	$\pm 1\%$
Number of ring magnets:	
dipole magnets	24 (connected in series)
quadrupole magnets	60 with 7 families
sextupole magnets	18 with 3 families
steering magnets	52
Number of rf cavities	12 (3 gaps per cavity)
Number of pulsed magnets:	
horizontal dipole magnets	
for the injection orbit bump	4 (connected in series)
horizontal/vertical dipole magnets	
for the injection painting	4/2
extraction kicker magnets	8 (2 thyratrons per magnet)

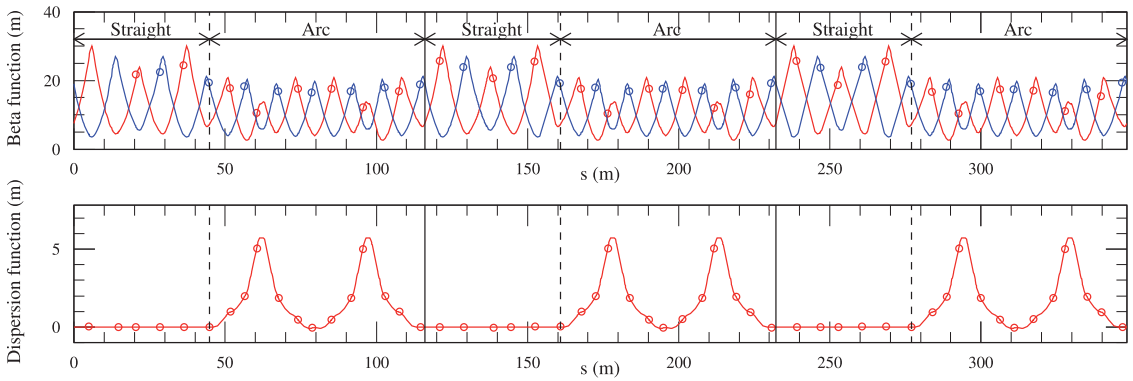

Fig. 2. Beta (upper) and dispersion (lower) functions along the ring. Red curves indicate horizontal components, blue curves indicate vertical components, and open circles indicate measured values.

rf frequency. The injection energy is 400 MeV, for which the transverse emittance and momentum spread of the injected beam are designed to be 4π mm mrad (unnormalized) and $\pm 0.1\%$ in full, respectively. The RCS spends 20 ms accelerating the injected 400 MeV protons up to 3 GeV. Most of the 3 GeV beam from the RCS is transported via the 3 GeV-to-neutron-target beam transport line (3-NBT) to the MLF. Part of the extraction beam (typically four pulses every several seconds) is transported via the 3–50 GeV beam transport line (3–50BT) to the MR for beam injection.

Figure 2 shows the optical functions along the RCS ring. As shown in Figs. 1 and 2, the RCS has a three-fold symmetric lattice over its circumference of 348.333 m. Each super-period consists of two 3-DOFO arc modules and a 3-DOFO long straight insertion, where DOFO describes a defocusing–focusing periodic cell. Each arc module has a missing-bend cell in which the horizontal dispersion is a maximum (6 m). Such a lattice structure of high dispersion gives a high transition energy ($\gamma_t = 9.2$ GeV), which is sufficiently far from the extraction energy of 3 GeV. This high-γ_t lattice obtained by the missing-bend technique is a unique feature of the RCS optics design. Three families of sextupole magnets utilized for chromatic correction are installed in the high-dispersion areas. On the other hand, the straight insertions are dispersion free. Injection and collimation systems are installed in the first straight section. Extraction and rf cavity systems are allocated in the second and third straight sections, respectively.

The RCS ring acceptance is 486π mm mrad for a possible momentum spread of $\pm 1\%$, for which the primary collimator aperture is set at 324π mm mrad. Such a large ratio (1.5) of ring acceptance to collimator aperture is necessary for localizing the particle losses in the collimator section and minimizing the irradiation of the remaining part around the ring in terms of keeping hands-on maintenance. To operate at the designed 1 MW beam power, an acceptable intensity loss is 3% in the region in which energy is injected, which is determined on the basis of the current collimator capability (4 kW).

3. Extraction system and kicker magnets in the RCS

3.1. Extraction system in the RCS

Figure 3 shows the extraction system in the second straight section of the RCS. It consists of eight pulsed kicker magnets and three DC septum magnets. Once the proton beams have been accelerated to a kinetic energy of 3 GeV, these kicker magnets give pulsed kicks to the two bunched beams to send them downstream to the septum magnets and then on to be extracted to the beam transport line.

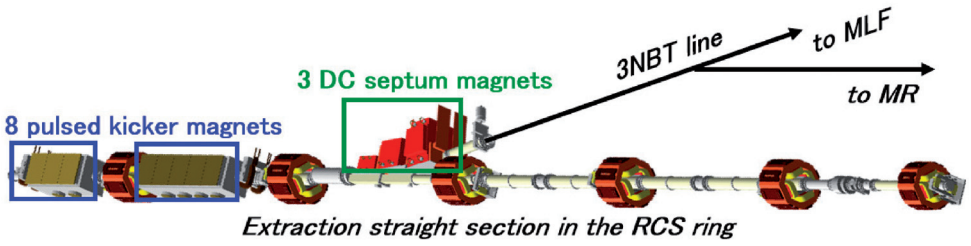

Fig. 3. Schematic view of the extraction system in the RCS.

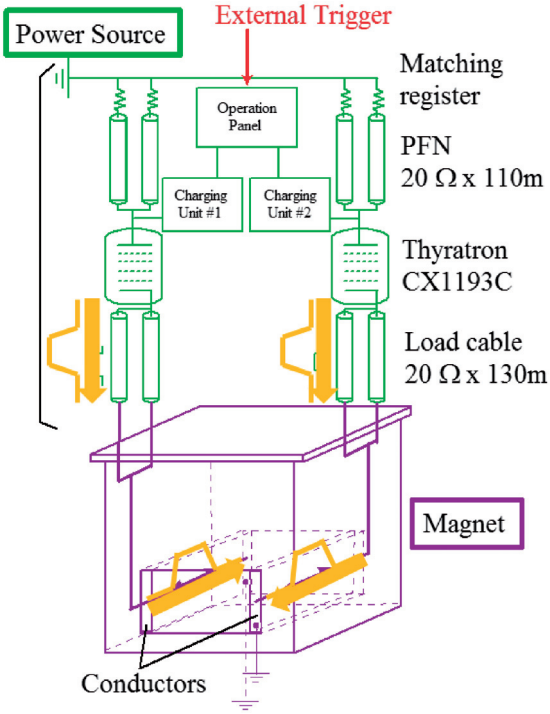

Fig. 4. Schematic diagram of the kicker magnet system. The green parts (top) show the power source. The purple parts (bottom) show the magnet. Orange arrows indicate the current flow.

The extracted two-bunch beam is delivered simultaneously to the MLF and MR with a repetition rate of 25 Hz.

3.2. Configuration of the kicker magnet system

The detailed configuration, power supply, and measured field of a kicker magnet have already been described in Ref. [9]. A schematic diagram of the RCS kicker-magnet system is shown in Fig. 4, the specifications of which are listed in Table 2. A kicker magnet consists of a twin-C distributed ferrite core with 20 units and two conductors in a vacuum. Figure 5 shows one of the units. The central earth plates are taken between the twin-C cores. High-voltage electrode plates are located both upstream and downstream of the core. On the other hand, the power source consists of two thyratrons, a pulse-forming network (PFN) and load cables, and matching registers. The thyratron in the power source is a high-power switch. The kicker magnet as shown in Fig. 4 is driven by two thyratrons via two conductors. The typical operational charging voltage of a thyratron is 60 kV, and the excitation current of a magnet with two thyratrons is 6 kA. As shown in Fig. 4, the two conductors

Table 2. Specifications of the RCS kicker system.

Numbers	8 (IDs 1–8)
Number of units per kicker	20
Repetition rate	25 Hz
Characteristic impedance	10 Ω
PFN	Coaxial cable (102 m)
Load cable	Same as PFN (130 m)
High-power switch	Thyratron CX1193C, e2V Ltd.
Number of switches per kicker	2 thyratrons
Operation charging voltage	60 kV
Operation output current	3 kA
Magnet structure	Distributed parameter line
Magnet core	Ni–Zn ferrite PE14, TDK Ltd.
Magnet gap height:	
S-type (IDs 3, 4, 5)	153 mm
M-type (IDs 2, 6)	173 mm
L-type (IDs 1, 7, 8)	199 mm
Magnet gap width	280 mm
Magnet length	638 mm
Magnetic field:	
S-type (IDs 3, 4, 5)	460 G
M-type (IDs 2, 6)	410 G
L-type (IDs 1, 7, 8)	360 G

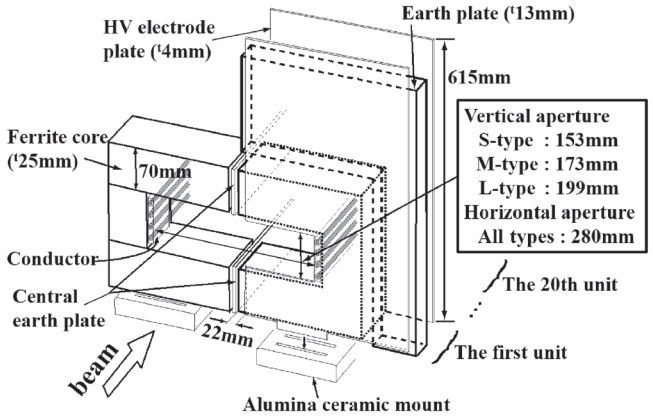

Fig. 5. Configuration of one unit of the kicker magnet as a conceptual design.

have excitation currents that flow in opposite directions, i.e., from downstream to upstream of one conductor and from upstream to downstream of the other. The eight kickers consist of three types (S-type: 3 kickers, M-type: 2 kickers, and L-type: 3 kickers), which are identified by vertical aperture gaps of 153 mm (S-type: kicker IDs 3, 4, and 5), 173 mm (M-type: kicker IDs 2 and 6), and 199 mm (L-type: kicker IDs 1, 7, and 8). The vertical gap height of each type depends on the vertical beta function at each kicker, where the field strength of each type is different. The horizontal gap width and the longitudinal length are 280 mm and 638 mm, respectively.

3.3. Measured magnetic field of a kicker magnet

We have measured the magnetic field of a kicker magnet by using a short search coil before installation into the ring. The time structures of the measured fields are shown in Fig. 6. The measured fields

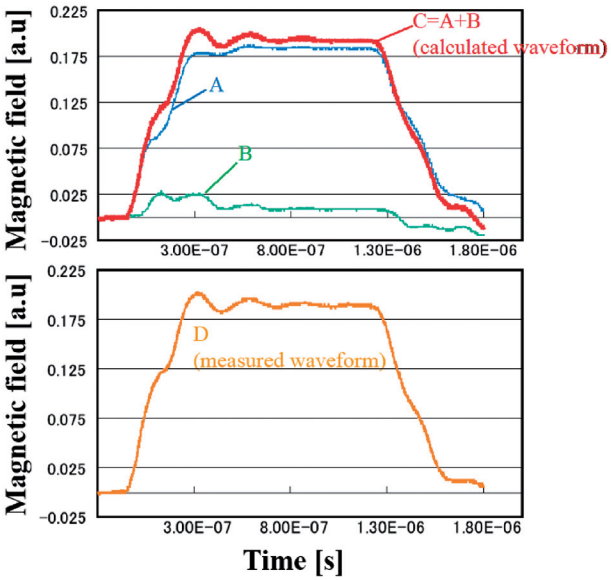

Fig. 6. Time structures of measured magnetic field. Fields A and B (upper panel) are the fields measured when the right- and left-hand-sides were excited, respectively. Field C (upper panel) is the sum of fields A and B. Field D (lower panel) is the time structure of the field measured when both sides were excited.

under conditions of right- and left-hand-side excitation are A and B, respectively, as shown in the upper panel of Fig. 6. For this field measurement, the short search coil was located in the ferrite core of the right-hand side. Field C is the sum of fields A and B. As shown in the lower panel of Fig. 6, field D is the field that was measured when both sides were excited. Field C is in good agreement with D, where field D is created by combining fields A and B. It was found that the flat-top disturbance that can be seen in the lower panel of Fig. 6 has two causes. Firstly, there is an impedance mismatch between the load cables and the corresponding magnet, which can be seen in the measured field A. Secondly, there is an effect from the magnetic field induced by the magnetic flux that penetrates from the opposite side of the ferrite core, which can be seen in the measured field B. Both conductors are driven simultaneously, but the excitation timing is delayed because of the longitudinal pass length of the loading current on the conductor. From the field measurements, the flatness of the field is estimated as roughly $\pm 3\%$. As a result, the flat top of the kicker magnetic field has a ringing structure, such as that measured for field D. The flatness of the kicker magnetic field affects the quality of the extracted beam directly just after the field rises.

4. Effect of kicker ringing on the extraction beam

Such ringing of the magnetic field causes the positional displacement of the extracted bunched beams. Therefore, to maintain the quality of the extracted beam, it is very important to compensate directly the effect of field ringing. In the RCS design stage, the required flatness and duration of the flat-top field were $\pm 1\%$ and 840 ns, respectively. However, the former was estimated as being $\pm 3\%$ from the field measurement. In the first RCS beam commissioning, cancellation of the field ringing was attempted by modifying the trigger timings of the kickers/thyratrons. The eight kickers were divided into two groups, namely the first group (kickers IDs 1, 3, 5, and 7) and the second group (kicker IDs 2, 4, 6, and 8). The trigger timing of the first group was fixed, whereas that of the second group was delayed by roughly 130 ns to cancel out the peaks and troughs of the field ringing. We refer here to this timing condition of the eight kickers as “reference timing delay.” By its use,

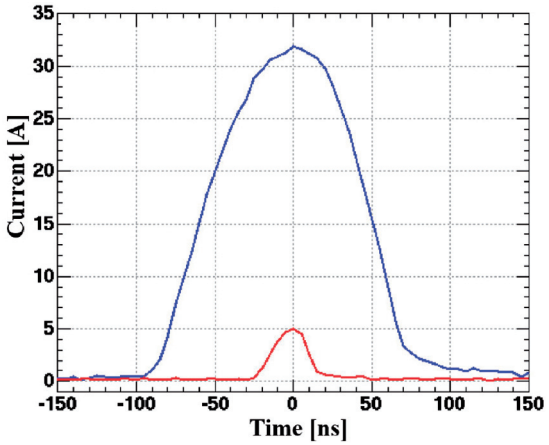

Fig. 7. Measured bunch shapes of the circulating beam just before beam extraction. The blue line is a typical bunch shape in user operation; the red line is the special bunch shape in this study.

a flatness of ±1% and a duration of 850 ns of the flat-top field were achieved, thereby satisfying the requirements of the first beam commissioning. A kicker field ringing of ±1% corresponds to an extracted-beam positional displacement of roughly ±4 mm. These results have already been reported and discussed in Ref. [10]. However, MLF users and MR operators require a higher field flatness and the same position of the two extracted bunches for higher-intensity operation to reduce the risk of target problems on the MLF and to suppress growth of the injection-beam emittance on the MR.

4.1. Beam-based measurement of the flat top

The flat-top uniformity of the kicker magnetic field directly affects the profile and position of the extracted beam. The trigger system of a kicker power supply consists of two timing modules. The first timing module controls the entire trigger timing of all the kicker magnets and thyratrons, and modifies the relationship between the extracted two-bunch beams and the kicker magnetic field. The second timing module also controls the individual trigger timing of each kicker magnet and thyratrons to access the time of flight of the beams between kickers and to cancel out the effect of the field ringing. To understand the flat-top uniformity on the total field of all kickers in the case of "reference timing delay," the uniformity was measured as the position displacements of the extracted beams by using a shorter bunched beam and scanning kicker-trigger timing of the first timing module. The measured bunch shapes of the extracted beams for typical and special shorter bunched beams are shown in Fig. 7. As shown in the figure, the bunch width and number of bunches of the typical proton beams in user operation were 180 ns and two bunches, respectively, whereas those of the special beams in this experiment were 30 ns and one bunch, respectively. The shorter bunched beam gives an extracted-beam position corresponding to the total kick angle on the flat top of the kicker magnets. The beam position monitor (BPM) is located downstream of the septum magnets in the extracted-beam transport line. To improve the resolution of the BPM for the shorter-pulsed/lower-intensity beam, the signal gain was 50 times higher than the typical one and the average number of shots was 10 shots, which improved the beam position fluctuation of ±2 mm to less than ±0.5 mm. The measured beam displacements Δx with scanning of the entire trigger timing is shown in Fig. 8. The timings of the first and second bunches in Fig. 8 are zero and 600 ns, respectively. The measured beam displacement Δx of the first bunch, which has a bunch length of 180 ns, ranges from −6.4 mm

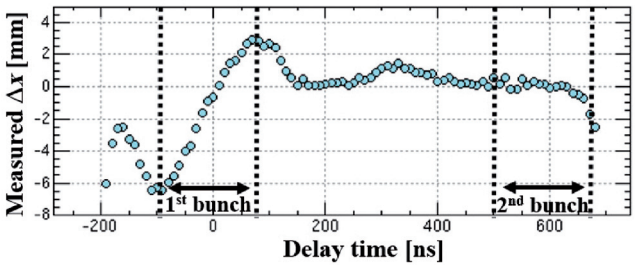

Fig. 8. Measured beam displacement (light blue dots) by using a shorter bunched beam and scanning the entire trigger timing. The regions within the dashed lines (black) describe the timings and widths of the first and second bunches, respectively.

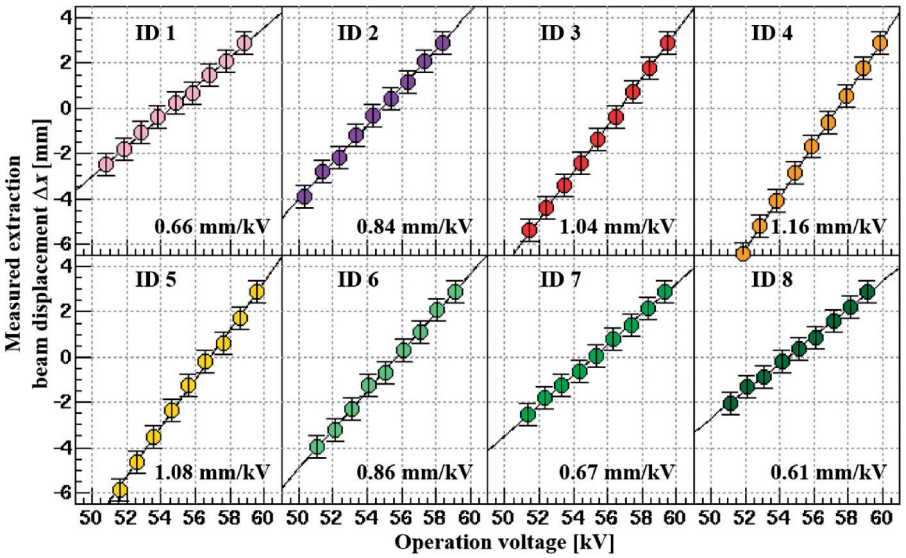

Fig. 9. Response measurements of extracted-beam displacement versus operational voltage kicker by kicker.

to +3.2 mm, corresponding to −1.6% to +0.8%. Hence, the beam displacement Δx of the first bunch was in excess of the requirement of ±1%.

4.2. Beam-based measurement of ringing effect kicker by kicker

From beam-based measurement of the kicker's flat top, the field ringing is not canceled out well and the effects of field ringing are not simple. Therefore, we need to perform two beam-based measurements, namely the beam displacement response for operational voltages and the ringing effect kicker by kicker. Firstly, we measured the response (Δx [mm]/ΔV [kV]) of the beam displacement for operational voltages kicker by kicker under fixed timing to understand the effect of voltage on the beam displacement. The measured responses and linearly fitted gradients kicker by kicker are shown in Fig. 9. The responses are linear and the gradients differ according to kicker type (S, M, and L). In particular, S-type kickers (kicker IDs 3, 4, and 5) have a lot of influence on the displacement. Secondly, we performed beam-based measurements of each field-ringing effect by scanning the individual trigger timings kicker by kicker to understand the ringing effect of each kicker on the extracted-beam displacements. The beam-based measurements of the ringing effect kicker by kicker are shown in Fig. 10. However, the rise time of the field differed according to kicker type. The first-peak timings of S and M type (kicker IDs 2 and 6) were delayed by 50 ns and 40 ns,

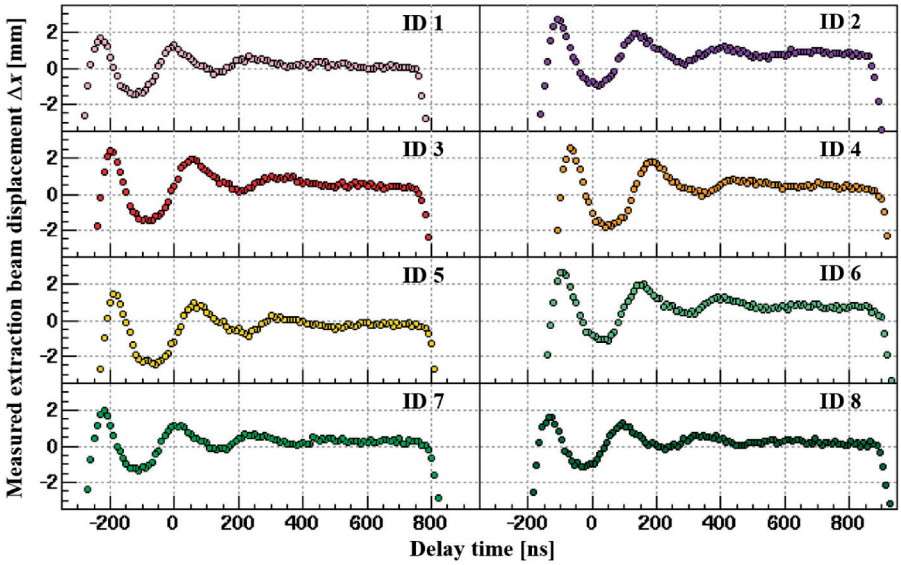

Fig. 10. Beam-based measurement of ringing effect kicker by kicker.

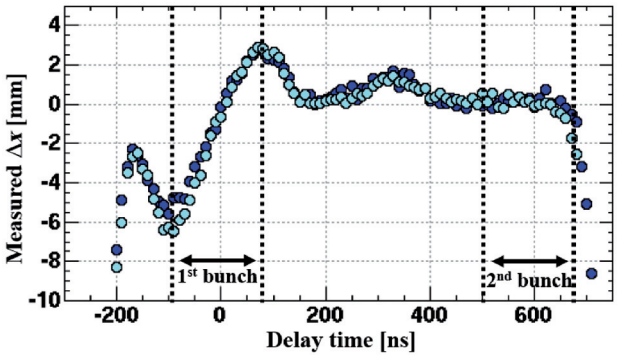

Fig. 11. Comparison between measured beam displacement Δx (light blue dots) by scanning the entire trigger timing and calculated beam displacement Δx_{sum} (blue dots) by summing the individually measured beam displacements. The regions within the dashed lines (black) describe the timings and widths of the first and second bunches.

respectively, in comparison with that of L type (kicker IDs 1, 7, and 8). Additionally, the peaks and troughs of the displacements had different amplitudes and widths. Therefore, we reasoned that it would be difficult to cancel out the field ringing using the reference timing delay. Nevertheless, we checked that these individual ringing effects are consistent with the measured beam displacements by scanning the entire trigger timing as shown in Fig. 8. A comparison between the measured beam displacement Δx by scanning the entire trigger timing and the calculated one Δx_{sum} by summing the individually measured beam displacements is shown in Fig. 11. These displacements are clearly consistent. Therefore, we can discuss better trigger timing among kickers based on the individually measured beam-displacement data to compensate for the ringing effect.

5. Kicker ringing compensation for higher extraction-beam quality

To compensate for the extracted-beam displacements caused by the kicker ringing field, we tried to modify the individual trigger timing of each kicker.

Table 3. Kicker trigger timing delay. Δt_0 is zero; $\Delta t_{\rm ref}$ is reference timing delay; $\Delta t_{\rm opt}$ is optimized timing delay.

Kicker ID	Δt_0	$\Delta t_{\rm ref}$	$\Delta t_{\rm opt}$
1	0 ns	0 ns	60 ns
2	0 ns	130 ns	110 ns
3	0 ns	0 ns	50 ns
4	0 ns	130 ns	160 ns
5	0 ns	0 ns	200 ns
6	0 ns	130 ns	100 ns
7	0 ns	0 ns	110 ns
8	0 ns	130 ns	90 ns

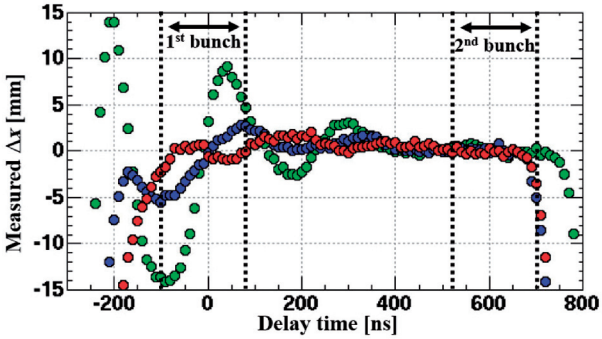

Fig. 12. Beam displacement $\Delta x_{\rm sum}$ calculated by summing the individually measured beam displacements for zero timing delay Δt_0 (green), reference timing delay $\Delta t_{\rm ref}$ (blue), and optimized timing delay $\Delta t_{\rm opt}$ (red). The regions within the dashed lines (black) describe the timings and widths of the first and second bunches.

5.1. Kicker ringing compensation by modification of trigger timing among kickers

The temporal structure of each kicker ringing was not simple and we could not adapt a classical method such as "least squares" to optimize the timing among the kickers. Instead, we used brute force to search the trigger timing of each kicker for further ringing compensation. The search involved checking the calculated beam displacement $\Delta x_{\rm sum}$ while shifting each timing datum of Fig. 10. The basic concept of the search is to cancel out the first trough of the ringing by using the first peak, while carefully checking the rise time of the total kicker field, because the rising field gives an unneeded kick to the circulating second bunched beam just before the beam extraction. Additionally, the trough is wider than the peak. So, the ratio of kickers with delayed timing (second group as described in Sect. 4) to kickers with basic timing (first group) changed from 4:4 (as for the reference timing) to 5:3. Subsequently, these timing delays were fine-tuned while checking the calculated beam displacements. The zero timing delay Δt_0, "reference timing delay" $\Delta t_{\rm ref}$, and optimized trigger delay $\Delta t_{\rm opt}$ arising from this search are listed in Table 3 for each kicker. The calculated beam displacements for each trigger delay (Δt_0, $\Delta t_{\rm ref}$, and $\Delta t_{\rm opt}$) are shown in Fig. 12. The beam displacement Δx with the optimized trigger delay $\Delta t_{\rm opt}$ was measured while scanning the entire trigger timing. A comparison between the measured beam displacement Δx by scanning the entire trigger timing and the calculated one $\Delta x_{\rm sum}$ by summing the individually measured beam displacements for the optimized trigger delay $\Delta t_{\rm opt}$ is shown Fig. 13. The measured beam displacement Δx is in good agreement with the calculated one $\Delta x_{\rm sum}$, and ranges from -1.2 mm to $+0.8$ mm, corresponding to -0.3% to $+0.2\%$.

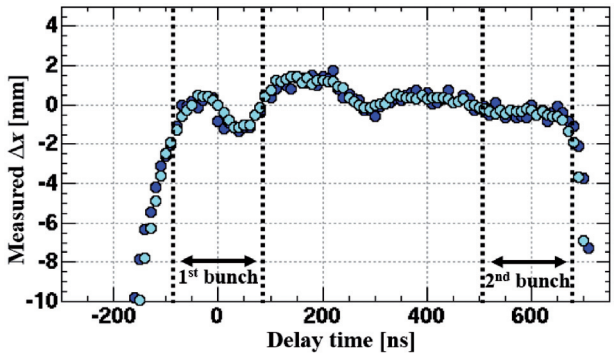

Fig. 13. Comparison between measured beam displacement Δx (light blue dots) by scanning the entire trigger timing and calculated beam displacement $\Delta x_{\rm sum}$ (dark blue dots) by summing the individually measured beam displacements for the optimized delay $\Delta t_{\rm opt}$ of each kicker. The regions within the dashed lines (black) describe the timings and widths of the first and second bunches.

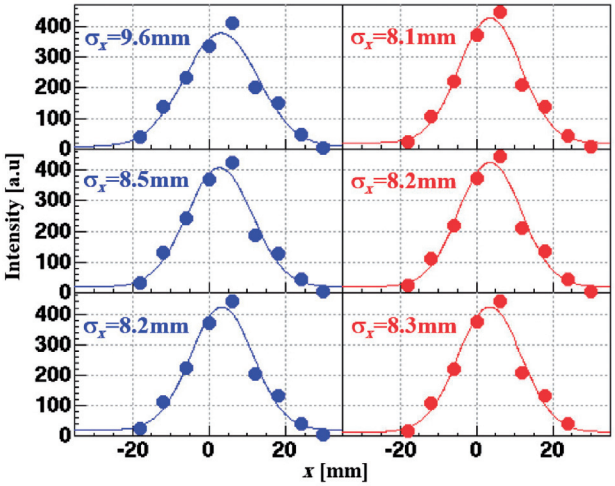

Fig. 14. Measured beam profiles of extracted first (left) and second (right) bunches at the extracted-beam transport line. The kicker conditions of the upper, middle, and lower panels are zero timing delay Δt_0, reference timing delay $\Delta t_{\rm ref}$, and optimized timing delay $\Delta t_{\rm opt}$, respectively. Standard deviation σ_x is obtained by fitting a Gaussian function.

The field-ringing effect of the kickers as shown in Fig. 12 was successfully compensated, fully satisfying the requirement of $\pm 1\%$.

5.2. Extracted-beam quality from beam profile measurements

To assess the quality of the extracted beam, we used a multi-wire profile monitor to measure the beam profile bunch-by-bunch for zero timing delay Δt_0, reference timing delay $\Delta t_{\rm ref}$, and optimized delay $\Delta t_{\rm opt}$ as described in Table 3; the profile monitor was located at the extracted-beam transport line (3-NBT). In this measurement, the beam profile was measured in single-bunch operation mode, in which the beam is injected in only single rf bucket of two ones, while switching the extraction timing between the first and second bunch timings to measure the profile of the second bunch as distinguished from that of the first bunch because it was necessary for the monitor response to be faster than the bunch interval. The measured beam profiles are shown in Fig. 14, where the standard deviation σ_x of each profile was obtained by fitting of a Gaussian function. As shown in Fig. 14, the

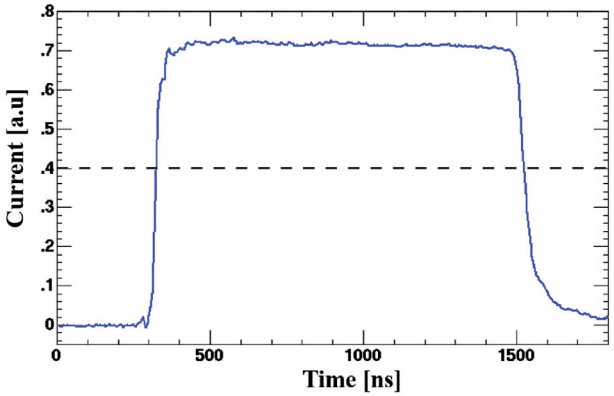

Fig. 15. Monitored output current of a single thyratron (solid blue line) and its current threshold (dashed black line).

measured beam profile of the first extracted bunch with zero timing delay Δt_0 is wider than the second extracted bunch; the kicker field ringing has an enormous effect on the first extracted bunch. The measured beam profile of the first extracted bunch with optimized delay $\Delta t_{\rm opt}$ is in good agreement with that of the second extracted bunch; the field-ringing effect of the kickers was successfully compensated by optimizing the trigger timing of each kicker to cancel out each ringing effect.

6. Higher stability of extracted beams

6.1. Beam-position drift with poorly conditioned thyratron

In the early phase of routine user operation, beam displacements in which only one bunch (first or second) shifted were common and stopped the operation temporarily. The position of the extracted beam drifted gradually from 0 to −25 mm over a period of minutes, whereupon beam losses occurred at the extracted-beam transport line. A system was adopted to detect beam displacement on the MLF target to protect it. We found that it is very important to maintain the trigger timing of each kicker to ensure the quality of the extracted beam. However, the output current of the thyratrons, which are the high-power switch in the kicker power supply, may have a timing drift due to gradual changes in the thyratron condition. Hence, we focused on the thyratron output current and built a system to monitor its waveform online. The waveform data of the output current from sixteen thyratrons were obtained by a digitizer every 2 s. The timings at which the current exceeded the threshold value (roughly half the maximum current) were detected as the rise timing $t_{\rm rise}$ of the current. The monitored output current of a single thyratron and the threshold level of the current are shown in Fig. 15. The 24 h trends of monitored $t_{\rm rise}$ for two thyratrons of kicker ID 8 are shown in Fig. 16. The output current of a poorly conditioned thyratron or one that is nearing failure (such as the second one in Fig. 16) shows considerable timing drift in excess of ±250 ns. In the case of the timing drift, the extracted beam of either the first or second bunch does not match the flat-top field of the kicker at which the beam displacement occurred.

6.2. Automatic drift correction of the thyratron output current

To resolve the problem of extracted-beam drift due to thyratron current drift, we developed the automatic drift-correction system in the current monitoring system. This new system obtained the drift timing value $\Delta t_{\rm rise}$ relative to the reference one for each thyratron at every monitoring event. In the early phase of this development, the trigger timing of each thyratron was controlled to match

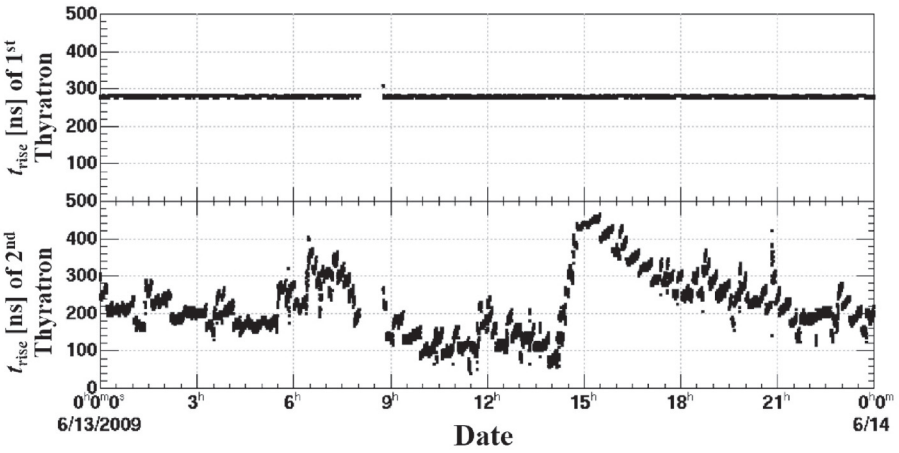

Fig. 16. Twenty-four hour trends of monitored rise timing t_{rise} of the first (upper) and second (lower) thyratrons (kicker ID 8).

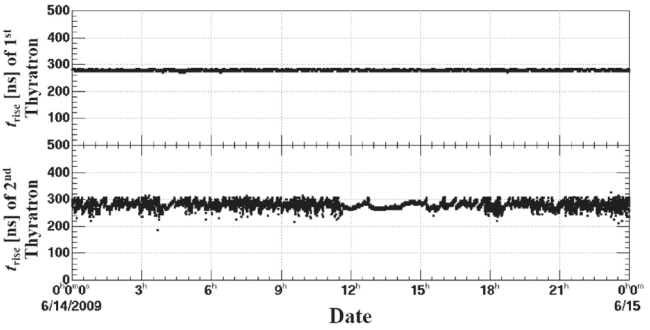

Fig. 17. Twenty-four hour trends of monitored rise timing t_{rise} of the first (upper) and second (lower) thyratrons (kicker ID 8) after introduction of the automatic drift-correction system.

the extracted beams automatically if Δt_{rise} exceeded ± 30 ns. The 24 h monitored t_{rise} trends of the two thyratrons for kicker ID 8 after introduction of the correction system in the early phase are shown in Fig. 17. As shown in the lower panel, the thyratron output-current drifts were successfully corrected by introducing the automatic monitoring and correction system, and the position of the extracted beam no longer drifts during routine user operation. At present, the range of Δt_{rise} is ± 10 ns. Additionally, this monitoring system gives us information about the thyratron condition, allowing scheduled replacement of those that are either in poor condition or nearing failure. We are now achieving highly stable currents such as that of the first thyratron of kicker ID 8 as shown in Fig. 17, and we are achieving higher stability of the extracted beams during routine RCS user operation.

7. Conclusions

In the RCS, we were aware from the results of magnetic-field measurements that the eight pulsed kicker magnets were experiencing flat-top field ringing of $\pm 3\%$. Both in the RCS and in other storage or accelerator rings, a method for compensating the displacement of extracted beams due to the field ringing of the kicker magnets is essential if the performance requirements are to be met, since the kicker-magnet system varies from facility to facility. The flat-top uniformity of the kicker magnetic field directly affects the profile and position of the extracted beam in the horizontal plane. In the

design stage of the RCS, the field flatness was required to be within ±1%. As such, the trigger timings of four of the kickers were already delayed by roughly 130 ns relative to the other four kickers in order to cancel out the peaks and troughs of the field ringing in the first stage of RCS beam commissioning. However, MLF users were requiring higher field flatness and a fixed position of the two extracted bunches to reduce the risk of target problems, and there was a need to suppress emittance growth during operational MR injection to achieve higher beam intensity.

To understand the flat-top uniformity of the total field of all the kickers, the uniformity was measured as the beam displacement of the extracted beams by using a shorter bunched beam and scanning the entire trigger timing of the eight kickers. The measured beam displacement Δx in the first bunch ranged from -6.4 mm to $+3.2$ mm, corresponding to -1.6% to $+0.8\%$, whereupon the field ringing was not canceled out sufficiently. To understand the ringing effect of each kicker, we performed beam-based measurement of each field-ringing effect by scanning the individual trigger timings kicker by kicker. As a result, we found that the peaks and troughs of the displacements caused by the ringing had different amplitudes and widths kicker by kicker. That meant that the time structure of each kicker ringing was not simple. The beam displacements Δx_{sum} calculated by summing the individually measured beam displacements on each kicker were in good agreement with Δx measured by scanning the entire trigger timing. So, we searched the trigger timing of each kicker by using the individual measurement data of beam displacements on each kicker. The basic concept of the search was to cancel out the first trough of the ringing by using the first peak, while carefully checking the rise time of the total kicker field that gave a kick to the circulating second bunched beam just before the beam extraction. The trough was wider than the peak. So, the ratio of kickers with delayed timing to kickers with basic timing changed from 4:4 (as with the reference timing) to 5:3. Additionally, these timing delays were fine-tuned while checking the calculated beam displacements. We obtained the optimized trigger delay Δt_{opt} by the search, and the beam displacement Δx was measured while scanning the entire trigger timing to confirm the effect of the ringing compensation. The measured beam displacement Δx was in good agreement with the calculated one Δx_{sum}, and ranged from -1.2 mm to $+0.8$ mm, corresponding to -0.3% to $+0.2\%$. As expected, the field-ringing effect of the kickers was successfully compensated, fully satisfying the requirement of ±1%. Furthermore, to assess the extracted-beam quality and the ringing compensation, extracted-beam profiles were measured bunch by bunch after optimization of the trigger timings. In the optimized delay Δt_{opt}, the measured beam profile of the first extracted bunch was in good agreement with that of the second extracted bunch, while the field-ringing effect of the kickers was successfully compensated by optimizing the trigger timing of each kicker to cancel out each ringing effect. We can now provide beams with higher quality by our procedures and techniques for field-ringing compensation, without any hardware upgrades or improvements.

We found that it is very important to maintain the trigger timing of each kicker to ensure the quality of the extracted beam. However, timing drifts of the output currents from the thyratron, which is a high-power switch in the power supply of the kicker, were causing the position of the extracted beam to drift. To resolve this problem, we developed a current monitor system and the output currents of the thyratrons had big timing drifts of ±250 ns over a period of minutes. Therefore, we upgraded the current monitoring system into an automatic drift-correction system. The system now controls the trigger timing of each thyratron to match the extracted beams automatically if the thyratron output current drifts. In doing so, the position of the extracted beam no longer drifts during routine user operation. Additionally, this monitoring system gives us information about the condition of the thyratron that allows us to make scheduled replacements of those that are either in poor condition

or nearing failure. Overall, we have now achieved higher stability of extracted beams during routine RCS user operation.

These essential techniques and procedures for higher quality and stability of the extracted beam can be applied to other storage or accelerator rings in the world.

Acknowledgements

We appreciate the J-PARC writing support group, which continuously encouraged us to write up this article. We would like to acknowledge all the members of the J-PARC RCS, LINAC, MR, and MLF groups for their indispensable support. Finally, we acknowledge the late Prof. A. Ando for his kind encouragement.

References

[1] Accelerator Technical Design Report for High-Intensity Proton Accelerator Facility Project, JAERI Report No. JAERI-Tech 2003-044 and KEK Report No. 2002-13.
[2] H. Hotchi et al., Phys. Rev. ST Accel. Beams **12**, 040402 (2009).
[3] H. Hotchi et al., Phys. Rev. ST Accel. Beams **15**, 040402 (2012).
[4] H. Harada et al., Proc. 52nd ICFA Advanced Beam Dynamics Workshop on High-Intensity and High-Brightness Hadron Beams, pp. 339–43 (2012).
[5] H. Hotchi, Proc. 2015 International Particle Accelerator Conference, pp. 1346–1348 (2015).
[6] H. Takada, T. Naoe, T. Kai, H. Kogawa, and K. Haga, Proc. 12th International Topical Meeting on Nuclear Applications of Accelerators, pp. 297–304 (2015).
[7] Y. Yamazaki, Proc. 2009 Particle Accelerator Conference, pp. 18–22 (2009).
[8] I. Sugai, Y. Takeda, M. Oyaizu, H. Kawakami, Y. Irie, A. Takagi, H. Hattori, and K. Kawasaki, Nucl. Instrum. Meth. Phys. Res. A **613**, 457 (2010).
[9] J. Kamiya, T. Ueno, and T. Takayanagi, IEEE Trans. Appl. Supercond. **16**, 1362 (2006).
[10] J. Kamiya, T. Takayanagi, and M. Watanabe Phys. Rev. ST Accel. Beams **12**, 072401 (2009).